Available online at www.sciencedirect.com
SCIENCE DIRECT
Journal of Power Sources 154 (2006) 95–105
JOURNAL OF POWER SOURCES
www.elsevier.com/locate/jpowsour

Ex situ visualization of liquid water transport in PEM fuel cell gas diffusion layers

S. Litster, D. Sinton, N. Djilali*

Institute for Integrated Energy Systems, University of Victoria, Victoria, BC, Canada V8W 3P6

Received 10 February 2005; accepted 12 March 2005
Available online 13 June 2005

Abstract

A novel fluorescence microscopy technique for visualizing the transport of liquid water in unsaturated hydrophobic fibrous media has been developed and is applied to the gas diffusion layer of a PEM fuel cell. In the experiments, fluorescein dye solution is pumped through the fibrous hydrophobic gas diffusion layer (GDL) and imaged with fluorescence microscopy. Transient image intensity data is correlated to the liquid surface height and is analyzed and presented in the form of three-dimensional reconstructions of the time-evolving gas/liquid interface inside the fibrous structure. The high spatial resolution of the visualization can resolve the dynamic transport of liquid water through distinct pathways, which helps to refine understanding regarding liquid water transport mechanism within these porous layers. The physical observations suggest that the water is not transported via a converging capillary tree as suggested in prior work and models. Rather, transport is dominated by fingering and channeling. Based on the physical insight obtained from the experiments, a new water transport scheme is proposed as the basis for developing improved models for water transport in hydrophobic gas diffusion layers.

Keywords: PEM fuel cell; Gas diffusion layer; Two-phase flow; Visualization; Microscale; Hydrophobic porous media; Fibrous media

1. Introduction

The accumulation of liquid product water in polymer electrolyte membrane (PEM) fuel cells currently limits the performance of these devices. Improved water management is needed to achieve the increase in power densities required for commercial acceptance of PEM fuel cells in transportation and other demanding applications. Liquid water accumulates in the porous gas diffusion layer (GDL) of the electrodes, restricting the access of reactant gases to catalyst sites. In addition, liquid water collects in the gas distribution channels and manifolding of the fuel cell stack. This flooding severely hinders the upper power limit by starving the supply of reactant gases. Moreover, liquid water flooding accelerates a number of fuel cell degradation mechanisms. Thus, significant performance gains, as well as lifetime enhancement, are possible with a better understanding of the liquid water transport phenomena present in the fuel cell.

In addition to the growing number of experimental attempts to understand the structure of the two-phase flow in PEM fuel cells [1–12], there has been many studies that have employed computational models [13–16]. Computational methods facilitate observation of liquid water transport in the regions of PEM fuel cells that are inaccessible to in situ measurements, such as the entire membrane electrode assembly. However, the reliability of the computational models is still limited by the lack of fundamental understanding of two-phase flow in fibrous porous media. In particular, a serious limitation when considering hydrophobic GDLs is the relationship used to model capillary flow. Typically, the capillary characteristics are modeled with a Leverett J-function in a form obtained experimentally by Udell [17] for soil-like porous media. In a recent review, Litster and Djilali [18] showed that there is a significant difference between the capillary relationship of Udell and that found for a Teflon coated porous media similar to a GDL. Thus, experimental characterization of capillary flow in GDLs is required before the accuracy of two-phase PEM fuel cell models can be verified. A brief review of GDL characteristics and of previous

* Corresponding author. Tel.: 1 250 721 6034; fax.: 1 250 721 6323.
E-mail address: ndjilali@uvic.ca (N. Djilali).

0378-7753/$ – see front matter © 2005 Elsevier B.V. All rights reserved.
doi:10.1016/j.jpowsour.2005.03.199

visualization studies is presented below prior to introducing the fluorescence-based technique developed for this study.

1.1. Gas diffusion layers

PEMFC electrodes feature two regions of porous media: the gas diffusion layer and the comparatively more dense catalyst layer. The gas diffusion layer is much thicker and more porous than the catalyst layer. The catalyst layer features significantly less void space because of the high content of required proton conducting ionomer (typically Nafion) [19]. Further variation exists in the properties of the gas diffusion layers employed in PEM fuel cells. Two structures, both consisting of carbon fibers, dominate the forms of gas diffusion layers currently available: carbon cloth and carbon paper. Carbon cloth is constructed of woven tows consisting of individual carbon fibers. Alternatively, carbon paper is formed from randomly laced carbon fibers.

Carbon paper electrodes feature a much more porous structure than their cloth counterparts. The mean pore diameter and porosity of carbon paper is approximately 35 μm and 85%, respectively. Carbon cloth values are much lower and difficult to quantify [20,21]. Both Mathias et al. [20] and Ihonen et al. [21] present detailed characterizations of gas diffusion layer materials. Another issue with carbon cloth is that it is only available in thicknesses between 350 and 1000 μm, whereas carbon paper is available in thicknesses as low as 90 μm. Additional thickness results in greater power losses due to Joule heating and increased resistance to mass transfer. In addition, the two gas diffusion layer structures vary by spatial uniformity and degree of anisotropy. Carbon cloth, because of its woven structure, is spatially heterogeneous on a macroscopic scale, whereas carbon paper is roughly spatially homogeneous due to its random lacing. Moreover, the woven nature of carbon cloth results in three degrees of macroscopic anisotropy, whereas carbon paper results in only two degrees. All three forms of porous media in PEM electrodes are summarized in Table 1.

Generally, gas diffusion layers are treated with a PTFE solution (Teflon) to increase the hydrophobicity of the medium. This aids water management in the electrode. The hydrophobicity causes water droplets to agglomerate and keeps liquid water from reentering the GDL after being expelled. Also, the hydrophobicity reduces condensation. Condensation occurs in PEM fuel cells because the fuel and oxidant gases are typically saturated with water vapor. It has been postulated that the condensation takes place in hydrophilic cracks in the carbon fibers [2].

1.2. Visualization of two-phase flow in PEMFC

Direct visualization of the transport of liquid water through the microscale pores of unsaturated gas diffusion layers has yet to be reported. This is largely due to the immense difficulty associated with making in situ measurements during the operation of PEM fuel cells. This difficulty is compounded by the requirements for microscale flow visualization, which include optical accessibility. However, there has been some progress using three methods:

1. Ex situ visualization of water droplets placed or condensed on an isolated GDL without net transport of the liquid [1–4].
2. Use of optically accessible flow fields to visualize the emergence of macrodroplets of liquid water from the surface of the GDL as well as their transport through the flow channels [1,5–7].
3. Implementation of radiography techniques to macroscopically visualize water distribution within an operational fuel cell [8–12].

The first approach furthers understanding of the interaction between liquid water and GDLs. Specifically, the level of hydrophobicity can be determined. However, external visualizations of static droplets do not resolve the bulk transport of liquid water within the porous structure. The last two techniques target the transport of liquid water within the fuel cell flow field. Nevertheless, these techniques do offer the opportunity of identifying locations where water is expelled from the GDL. The critical nature of the problem and the attendant challenges are highlighted by the fact that all the studies referenced above were published in the last 2 years.

1.2.1. Ex situ visualization

To visualize the contact angle between liquid water and gas diffusion layers, Tüber et al. [1] and Pasaogullari and Wang [3] captured images of liquid droplets resting on the surfaces of GDLs with varying hydrophobicity. Lim and Wang [4] conducted a study of hydrophobic polymer content in GDLs, quantifying the hydrophobicity with an adapted capillary rise method. They also introduced an additional method of visualizing the contact angle. By utilizing a microscope and a CCD camera, Pasaogullari and Wang visualized the rise height on the exterior surface of a GDL dipped into a bath of heated water.

Nam and Kaviany achieved, with the aid of environmental scanning electron microscopy (ESEM), the closest realization of microscale liquid water transport visualization in an

Table 1
Summary of porous media in PEM electrodes [20,21]

Porous media	Spatial uniformity	Dimension of anisotropy	Porosity (%)	Mean pore diameter (μm)	Thickness (μm)
Catalyst layer	Homogeneous	Isotropic	5–55	~ 1	~ 15
Carbon cloth	Heterogeneous	3D	30–40	∼10	350–1000
Carbon paper	Homogeneous	2D	70–90	∼30–40	90–350

unsaturated GDL. Their imaging presented the distribution of liquid droplets that had condensed on the fibers of a hydrophobic GDL. ESEM is a type of SEM that places the sample in a low-pressure condensing environment such as water vapor. Condensation is induced by incrementally increasing pressure. Though this visualization offers insight into the distribution of condensation sites within a GDL, it does not provide visualization of the bulk transport of liquid water through the GDL. This study provided nonetheless some important insight into the local motion of the water microdroplets and their coalescence inside hydrophobic fibrous media.

1.2.2. Optically accessible flow fields

Optically accessible flow fields allow fuel cell researchers to visualize the transport of liquid water through the gas delivery channels. These techniques rely on the use of CCD cameras to record phase distribution. Water transport visualization in flow fields has been reported by the research groups at Penn State [5,7], and at the Fraunhofer Institute [1,6]. This form of visualization can aid in the understanding of liquid flows in unsaturated GDLs by resolving the subtleties of droplet formation on the surface of the GDL and the distribution of emergence sites. However, these visualizations provide little insight into the behavior or distribution of liquid water within the GDL.

1.2.3. Radiography

By constructing a fuel cell out of non-magnetic materials, Tsushima et al. [8] used MRI to visualize the transport of liquid water across a polymer electrolyte membrane during operation. The nature of the MRI technique restricted tests to a wider than average membrane. However, this did provide insight into the otherwise invisible transport of water at the gas diffusion electrode/membrane interface. Feindel et al. [9] recently overcame the limitation of visualizing liquid water in the flow field with MRI by fabricating flow fields from machined Delrin with gold contacts. But because graphite GDLs were still required, the water content in the GDL could not be adequately visualized.

Neutron imaging has shown potential for visual inspection of transport of liquid water in an operating fuel cell. The relatively higher sensitivity of neutron transmission to the hydrogen in liquid water than to metals makes it ideal for monitoring two-phase flows. Material limitations are few relative to other tomography and radiography techniques. The use of neutron imaging for visualizing liquid water transport in fuel cells was first reported by Satija et al. [10]. They utilized the National Institute of Standards and Technology's (NIST) neutron beam line and were able to generate videos of water transport by capturing 1000 images at 2 s intervals. However, because of the nature of radiography, only planar integrals of water content were available. This feature makes visualization of through-plane flow in individual pores in a GDL very difficult. Satija et al. used tomography to reconstruct the three-dimensional structure of a dry cell not in operation. A significant disadvantage of tomography for flow visualization of water transport in GDLs is the temporal resolution, which is on the order of seconds for good quality images.

Recently, Kramer et al. [11] published their findings employing neutron radiography to perform PEM fuel cell diagnostics. Their paper presents a number of advancements in data treatment and water quantification. Pekula et al. [12] have also recently presented results of an experimental analysis of water transport in an operating PEM fuel cell. Notably, they were able to acquire images at a rate of 30 frames s^{-1}, which is a significant improvement over the values reported by Satija et al. and Kramer et al. The effect of this higher frame rate on image quality was not discussed. Nevertheless, Pekula et al. were able to identify water entrapment in recirculation zones located in the bends of the flow field.

There are three distinct reasons why most visualization techniques so far have been unable to achieve visualization of two-phase flow within GDLs.

1. GDLs are optically opaque.
2. GDLs are formed of graphite.
3. GDLs have characteristic geometries with length scales under 50 μm.

The opacity of GDLs eliminates methods necessitating complete optical access, such as conventional microparticle image velocimetry (PIV) , photobleaching, caged fluorescence, and other velocimetry techniques that track particles or discrete fluid volumes [22]. The second issue is that the presence of graphite limits the use of techniques that employ X-ray transmission [10] such as X-ray micro-PIV [23]). The third point rules out the use of transmission radiography techniques due to typical resolutions greater than the mean GDL pore diameters of 35 μm. In addition, radiography presents difficulties in resolving flow within a single pore because of the integral image. It is likely that with modest improvements in resolution the planar neutron imaging technique of Satija et al. [10] would be very valuable for GDL analysis. The complexity and cost of neutron imaging, however, present additional challenges.

In this paper we present a novel method for visualizing the transport of liquid water in unsaturated gas diffusion layers. The visualization is sought to improve computational models and provide a new means to evaluate GDLs. To achieve these goals, fluorescence microscopy is employed to visualize fluorescein dye (water-based) pumped through the GDL structure. This method overcomes the majority of obstacles faced by other methods, but has some limitations. Through image processing, three-dimensional renderings of the temporal evolution of the gas/liquid interface are constructed. The experimental observations are used to postulate a new water transport mechanism in hydrophobic fibrous GDLs.

2. Experimental

Ex situ visualization of liquid water transport in gas diffusion layers is accomplished with fluorescence microscopy.

Fluorescence imaging is a form of scalar-based flow visualization in which the properties of a flow field are elucidated with a conserved scalar. Fluorescence imaging includes a multitude of techniques employing certain molecules that emit a photon immediately after being excited by electromagnetic radiation. Polyaromatic hydrocarbons are commonly employed for fluorescence imaging [22]. The fluorescence process can be idealized in three steps: absorbance, dissipation, and emission. First, the molecule absorbs a photon from an excitation beam (blue light, $\lambda = 488$ nm). Second, the excited state achieved from absorbing the photon dissipates to the surrounding environment. Third, a photon of lower energy is emitted (green light, $\lambda > 510$ nm). Quantitative fluorescence imaging is a well-developed field. For example, the local intensity of the emitted green light can be correlated to the concentration of fluorescent dye to quantify mixing [24].

A description follows of the gas diffusion layer, the experimental apparatus and the image acquisition and processing techniques used in this study.

2.1. Gas diffusion layer

The present analysis employed a Toray TGP-H-060 nonwoven fibrous gas diffusion layer. The GDL is coated with PTFE for the desired hydrophobic surface. The PTFE content of the GDL studied was 10 wt.%. The TGP-H-060 GDL features a thickness of 190 μm. The mean pore diameter of this layer has been determined to be approximately 40 μm from capillary flow porometry and mercury porosimetry [20]. Moreover, a mean fiber diameter of 8 μm was been determined from microscope images. An image of this layer, captured with an optical microscope, is presented in Fig. 1.

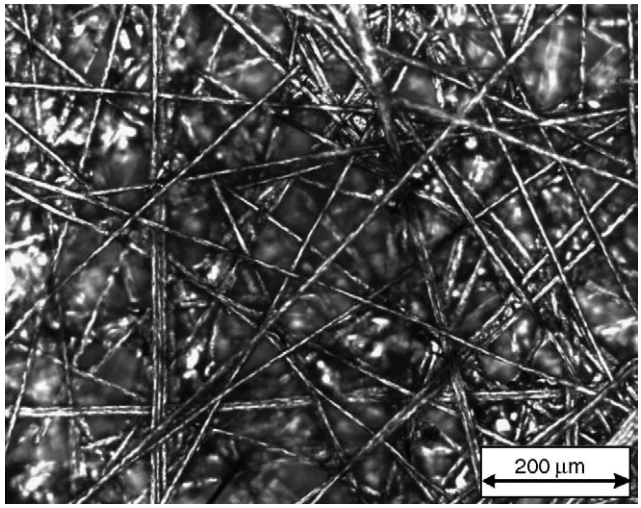

Fig. 1. Optical microscope image of a Toray TGP-H-060 gas diffusion layer with a PTFE content of 10 wt.%.

2.2. Apparatus

The experimental apparatus consisted of an optical microscope arranged for fluorescence microscopy, a cooled CCD camera, a numerically-controlled syringe pump, and an assembly for pumping fluorescein dye through the GDL. A schematic of the experimental apparatus is shown in Fig. 2.

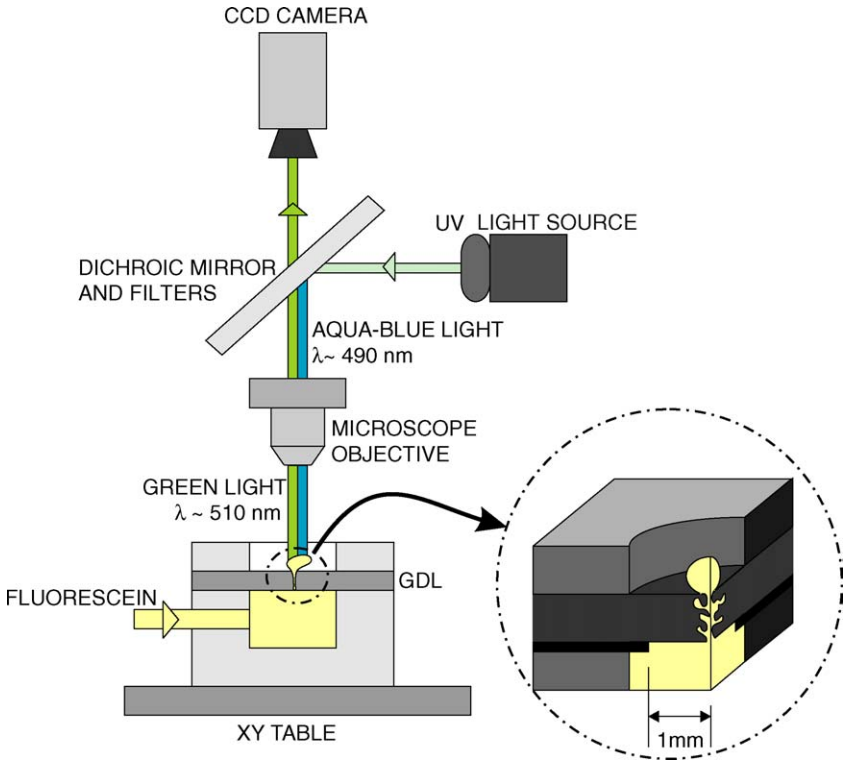

Fig. 2. Schematic of the experimental apparatus.

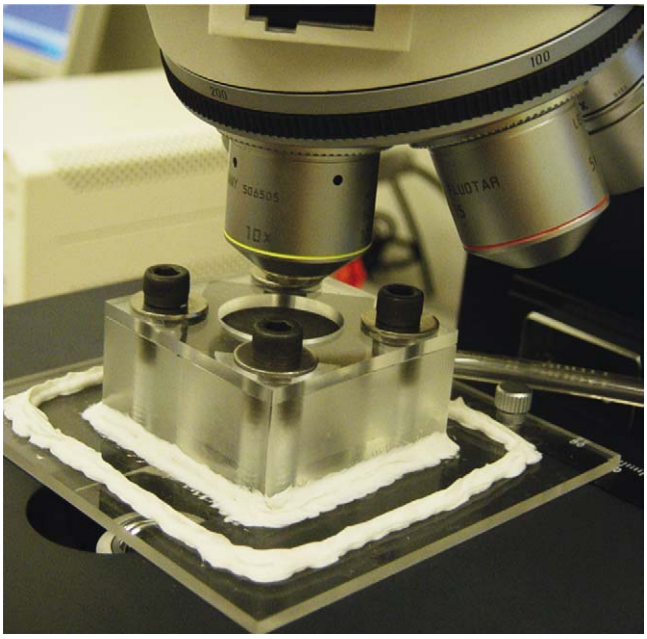

Fig. 3. GDL holding assembly.

The GDL is held in place above the fluid reservoir by the compression of a screwed-on top plate. The top plate also effectively seals the edge of the GDL. In order to concentrate water transport at the center of the GDL, the bottom surface was masked except for a ≈ 2 mm ×2 mm window in the center of the apparatus. A photograph of the GDL assembly is shown in Fig. 3.

Images were captured with an upright Leica Microsystems DM LM optical microscope featuring a cooled CCD camera. Magnification was achieved using an objective with 5× magnification and a numerical aperture (NA) of 0.15. These characteristics result in a depth of field (d_{field}) equal to 23 μm.

$$d_{\text{field}} = \frac{\lambda}{\text{NA}^2} = \frac{510\,\text{nm}}{0.15^2} = 23\ \mu m. \quad (1)$$

The depth of field is an important parameter in the present study because it corresponds to the though-plane height of the gas diffusion layer that can be in focus simultaneously. With respect to the fluorescent dye, the depth of field is a measure of the vertical extent of the imaging volume in which the fluorescence signal is integrated. Since the numerical aperture of microscope objectives generally increases with magnification, greater lateral resolution arrives at the cost of a reduced depth of field. For this reason, a low magnification of 5× was chosen to maximize depth of field, while maintaining adequate lateral resolution. The trade-off between the range of the fluid height measurement and the planar resolution of the area in focus is a limitation of this method.

2.3. Image acquisition and processing

To visualize the liquid transport, a solution of water and fluorescein is pumped through the plane of the GDL and imaged with fluorescence microscopy. The fluorescent dye employed here was fluorescein, 332 MW (Molecular Probes). The dye was dissolved to a concentration of 0.5 mM in pure water. Due to the imaging intensity of the fluorophores this relatively low concentration provided ample signal and contributed negligibly to the physical properties of the solution. With respect to surface properties, by imaging droplets on the GDL surface it was determined that both pure water and water with the fluorescein marker exhibited similar wetting behavior.

The path of the liquid fluorescein dye evolves as the pressure in the fluid reservoir increases. The rate of pressure increase is minimized and controlled by the pumping rate via a syringe pump. Because of the slow pressure increase, observations of the step-by-step evolution of the fluid path are made. Images of the fluorescein dye are captured at an adequate time interval (0.25 s) to reveal the various paths of the water inside the GDL. Subsequent image analysis correlates the light intensity to the relative height of the liquid water surface. Additional image processing provides three-dimensional renditions of the liquid water surface and the surface velocities.

In many studies, such as that by Oddy et al. [24], the fluorescence intensity field imaged is correlated to the concentration field of the fluorescent marker. In the present study, the presence of fluorescence signal differentiates the liquid phase from the gas phase. Since the concentration of fluorescent dye in the liquid is uniform, the local relative intensity of the fluorescence signal imaged is assumed to vary proportionally to the depth of excited fluorescein. Herein, the two-dimensional intensity array recorded by the CCD camera is linearly correlated to the relative height of the gas/liquid interface.

The correlation between the range of the height and the range of the image intensity is derived from the depth of field and experimental observations. The observable range of the surface height presented herein is 30 μm, slightly greater than the nominal 23 μm depth of field. This estimated range is supported by observations of the fluorescein dye within the height of three to four 8 μm diameter fibers. The linear correlation between surface height (η) and the 8-bit intensity data (I) is expressed as:

$$\eta = \frac{30 \times 10^{-6}\,\text{m}}{255} I \quad (2)$$

Prior to correlating the image intensities to heights, images were processed with a smoothing filter to reduce high frequency noise in the image. The signal-to-noise ratio (SNR) of this method is relatively high when little fluorescein is present. However, as more fluorescein appears, the reflectivity of the carbon fibers becomes significant and decreases the SNR to some extent. The contribution of reflected light to the signal was effectively removed by thresholding. The digital resolution of the acquired images is 325 × 258 pixels resulting in a spatial resolution of 5.35 μm pixel^{-1}.

3. Results and discussion

Time-sequenced images of the fluorescein dye traveling through the GDL are presented in Figs. 4 and 5. The images are those captured directly using fluorescence microscopy with the image contrast inverted for clarity. A three-dimensional rendering of the image intensity data is displayed next to each captured image. The three-dimensional renderings feature a magnified vertical scale to improve the visibility of surface features. The images and renderings are presented at intervals of 14.5 s.

In the images at the start of the sequence there is a very low disperse signal emanating from within the GDL. Nevertheless, the largest signal in the first two slides is located at the center, indicating the location of the liquid surface. On the third slide, however, there is a sudden appearance of flouresscein dye closer to the top edge of the images. Subsequent images and three-dimensional renderings indicate that the

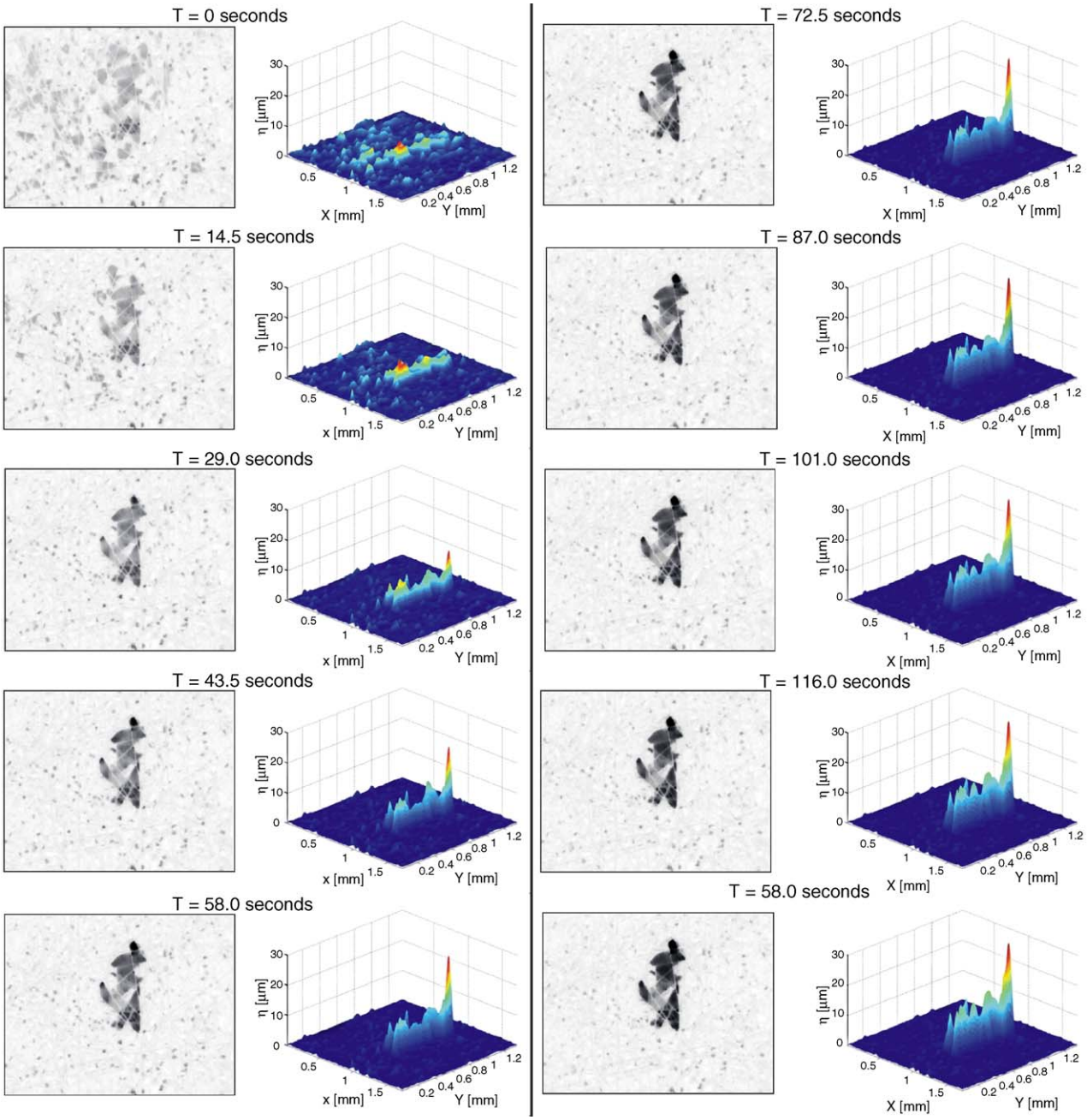

Fig. 4. Time sequenced digital images of dye transport in the GDL and corresponding three-dimensional renderings. Contrast of digital images is inverted.

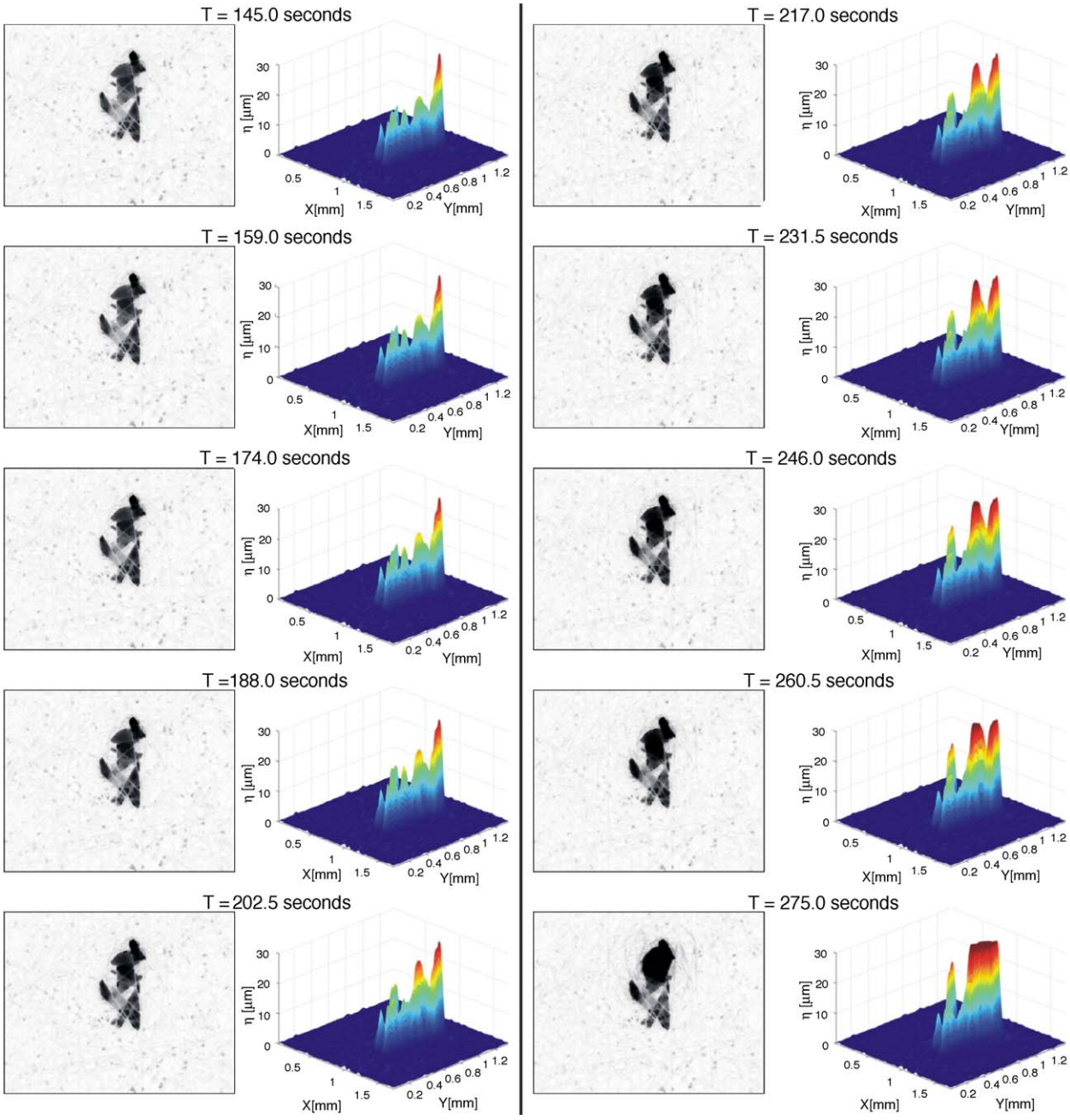

Fig. 5. Continuation of the time sequenced digital images of dye transport in the GDL and corresponding three-dimensional representations from Fig. 4.

surface of the fluid reached a particularly small fiber cross-section and its further progression is restricted by the strong capillary pressure.

After the initial advance of water, a number of additional paths develop more slowly in the upward direction. It becomes evident in the images and renderings later in the sequence that there is one dominant fluid path located below the path that first emerged. At times between 159.5 and 202.5 s, the liquid rises through this dominant path, while the fluid in an adjacent path falls. This is attributed to a local decrease in pressure as the fluid in the dominant path rises quickly having broken through a local constriction.

In the final images and three-dimensional renderings it becomes evident that the liquid is on the verge of breaking through the GDL. In the last image, it appears the two top fluid paths have merged into one large path. This is because the two paths have merged at the surface of the GDL. Immediately after the last image in Fig. 5, a spherical droplet forms on the

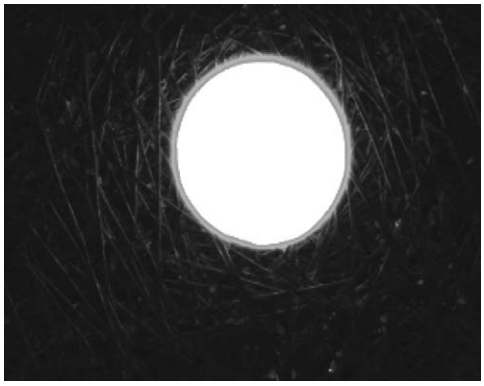

Fig. 6. Raw fluorescence microscopy image of a droplet immediately after breakthrough.

surface the GDL. A raw fluorescence microscopy image of this droplet is shown in Fig. 6. This figure clearly shows the reflectivity of the fibers.

3.1. Analysis of distinct flow paths

To further identify the dynamic interaction between adjacent flow paths, five of them have been selected for further analysis. Fig. 7, which is a contour plot of filter image intensity at a time of 175 s, presents the five flow paths that have been chosen. The paths discussed previously are paths 1–3. Path 1 is the route of the first liquid advance. Path 2 is the dominant pathway, where the liquid breaks out of the GDL. Path 3 is the pathway, where the liquid surface is shown to fall, while the surface in path 2 quickly rises (see Fig. 5).

Fig. 8 presents the surface height of each distinct path versus time. This plot features a much higher temporal resolution than that of the snapshots in Figs. 4 and 5. The higher temporal resolution allows analysis of more rapid phenomena . For example, the rapid rise of path 1 is clearly resolved in Fig. 8. Notable features of Fig. 8 include the jump in the height of path 2 when path 1 stops rising at a time of 60 s. Moreover, the connection between the rise of path 2 and the fall of path 3 at 200 s is well defined. The possibility of this contrast being an artifact of the imaging can be eliminated. This conclusion is made because of the negligible effect of path 2's quick rise at 200 s on the other paths. The dominant influence of path 2 on path 3 can be attributed to their close proximity and apparent high level of connectivity.

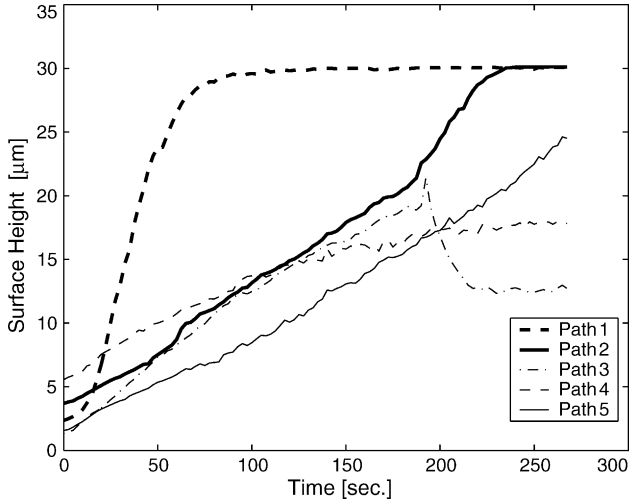

Fig. 8. The height of each path defined in Fig. 7 vs. time.

For improved analysis of path connectivity, the gradient of the fluid surface height with respect to time is presented. Fig. 9 presents a contour plot of the vertical velocity of the fluid surface at 194 s. This point in time corresponds to the interdependent rise and fall of paths 2 and 3, respectively. This plot additionally resolves any concerns that the contrast of these two paths might be an imaging artifact by clearly

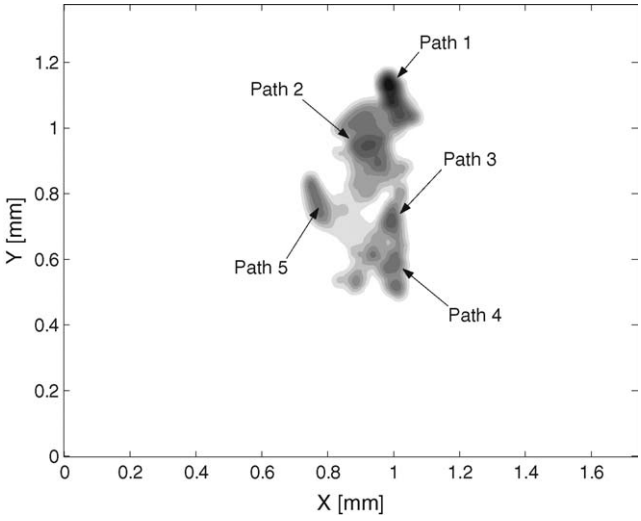

Fig. 7. Contour plot of the filtered image intensity at a time of 175 s that identifies the distinct flow paths analyzed in Figs. 8 and 10.

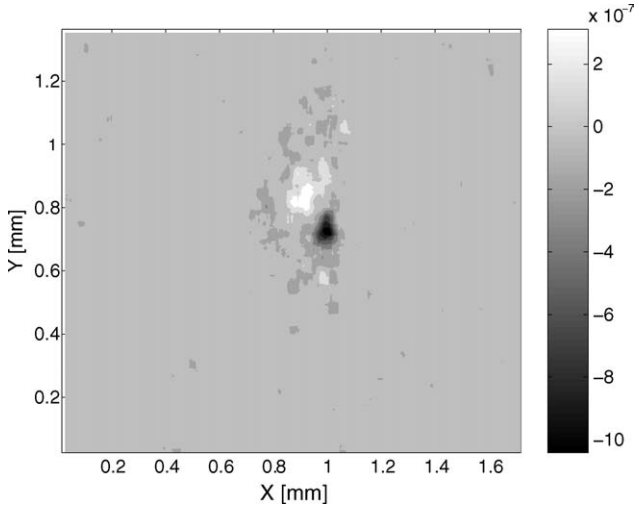

Fig. 9. Contour of the liquid surface vertical velocity at $t = 194$ s.

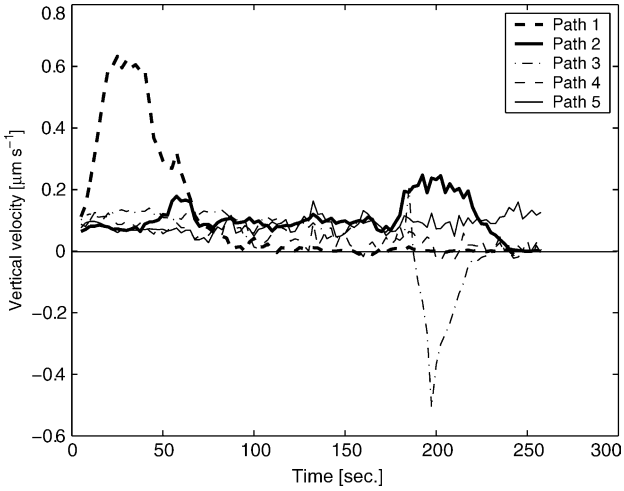

Fig. 10. The vertical velocity of each path defined in Fig. 7 vs. time.

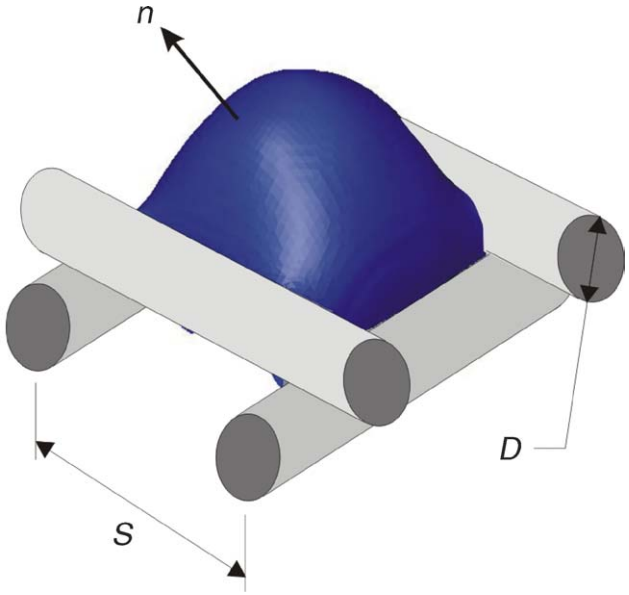

Fig. 11. Illustration of a liquid interface in the cross-section of four intersecting fibers.

showing localized areas of positive (path 2) and negative (path 3) velocity.

Plots of the fluid interface vertical velocity in each distinct path are shown in Fig. 10. Though calculating gradients amplifies errors from signal noise and processing, the flow features shown in Fig. 8 remain evident. A spike in the velocity of path 2 when path 1 reaches the GDL surface at a time of 60 s is present. Also, the sharp drop in velocity of path 3 corresponding to the increased velocity of path 2 is clear.

4. Further discussion: transport mechanism

From the preceding analysis of the acquired visualization data, the mechanism for water transport through the gas diffusion layers of PEM fuel cells is inferred. Fig. 11 is an illustration of the liquid interface generated when the liquid surface passes through the cross-section generated by four intersecting hydrophobic fibers. The capillary pressure (P_c), which is the jump in pressure across the gas/liquid interface due the fluid surface curvature (κ), is approximated by:

$$P_c = \sigma\kappa \tag{3}$$

where

$$\kappa = \nabla n \tag{4}$$

where n is the surface normal and σ is the interfacial tension. For a square intersection of four fibers, the curvature can be approximated with the contact angle (θ), fiber spacing (S) and fiber diameter (D):

$$P_c = \frac{2\sigma\cos(\theta)}{S - D} \tag{5}$$

Assuming well-dispersed PTFE coating (uniform θ), the transport within the GDL is a process of pressure buildup and breakthrough. This process results from the main resistance to the progression of the interface being capillary forces in the hydrophobic structure. As water production in the catalyst layer increases the pressure in the liquid, the fluid surface slowly passes through the constrictions of the cross-sections generated by intersecting fibers. When the water has passed halfway through each constriction, the curvature of the surface decreases due to the expanding radius of the surface. Thus, the liquid pressure at the interface drops and induces hydrodynamic flow in the direction of the expanding surface. Subsequently, the liquid expands rapidly above this cross-section until the fluid interface contacts the next set of fiber intersections. The process then begins again. The fluid will preferentially pass through the fiber cross-sections featuring the greatest spacing, as this reduces capillary pressure resistance. An idealized schematic of the flow mechanism is illustrated for the entire thickness of a GDL in Fig. 12.

The transport mechanism depicted in Fig. 12 is consistent with the experimental observations presented earlier on the evolution of water in the various paths. The mechanism presented here is different from that proposed by Nam and Kaviany [2] and Pasaogullari and Wang [3]. Both of these works presented the flow as an “upside-down tree” capillary network. These schematics feature a high number of small capillaries dispersed evenly within the GDL that converge into larger capillaries and eventually result in one very large capillary that reaches the surface. However, the observations herein promote the belief that the transport is dominated by fingering and channeling and features numerous “dead ends”, where water transport recedes when an adjacent breakthrough channel forms. The visualization supports this hypothesis because the dominant path is no larger than an average-sized fiber cross-section. In addition, after the liquid has broken through a constriction it is seen to fill the entire void space

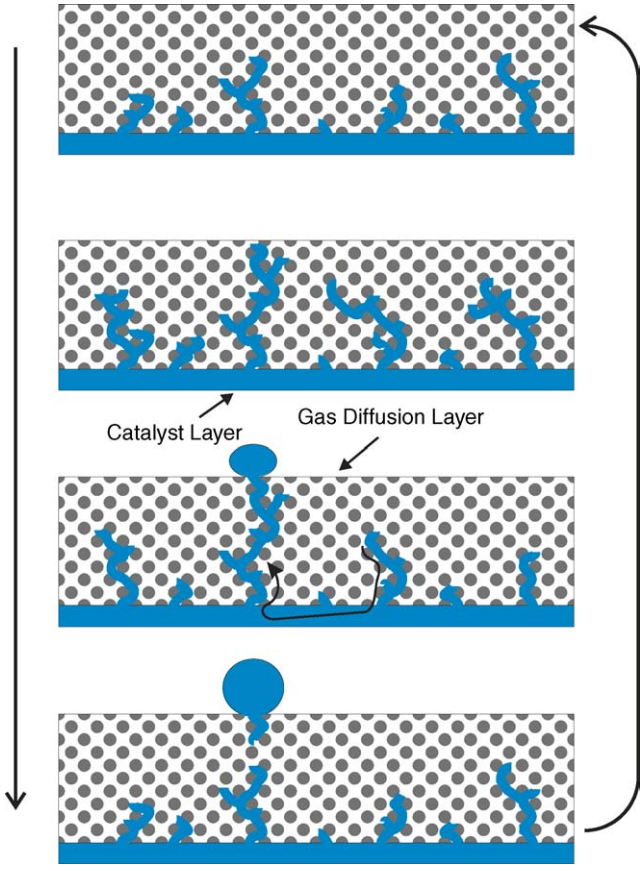

Fig. 12. Idealized schematic of the mechanism for liquid water transport in PEM fuel cell gas diffusion layers.

surrounded by other fiber cross-sections. Thus, the convergence of small capillaries into successively larger ones is not the observed mechanism in the non-woven gas diffusion layers.

5. Conclusion

Fluorescence microscopy has been employed with a novel methodology to provide new insight into the dynamic behavior and distribution of liquid water as it is transported through the gas diffusion layers in PEM fuel cells. The new quantitative visualization methodology consists of pumping fluorescein dye through a GDL and correlating the light intensity emitted by the fluorescein dye to the height of the fluid surface. The visualizations obtained with image processing enabled an analysis of the connectivity and interdependence of the liquid motion in several distinct flow paths. The results of the analysis prompted the author to revisit the previously adopted transport mechanism hypothesis. The experimental observations led to the postulation of the primary mechanism for liquid water transport in hydrophobic GDLs. The new hypothesis should prove valuable in the development of models for predicting liquid water transport in operating fuel cells. Moreover, the novel experimental methodology provides an additional method for further characterization of gas diffusion layers.

Acknowledgements

This work was conducted with the support of discovery grants (ND, DS) and a Canada graduate scholarship (SL) from the Natural Science and Engineering Council of Canada, as well as infrastructure funds from Western Economic Diversification Canada.

References

[1] K. Tüber, D. Pócza, C. Hebling, Visualization of water buildup in the cathode of a transparent PEM fuel cell, J. Power Sources 124 (2) (2003) 403–414.
[2] J.H. Nam, M. Kaviany, Effective diffusivity and water-saturation distribution in single- and two layer PEMFC diffusion medium, Int. J. Heat Mass Transf. 46 (2003) 4595–4611.
[3] U. Pasaogullari, C.Y. Wang, Liquid water transport in gas diffusion layer of polymer electrolyte fuel cells, J. Electochem. Soc. 151 (3) (2004) A399–A406.
[4] C. Lim, C.Y. Wang, Effects of hydrophobic polymer content in gdl on power performance of a PEM fuel cell, Electrochim. Acta 49 (2004) 4149–4156.
[5] G.Q. Lu, C.Y. Wang, Electrochemical and flow characterization of a direct methanol fuel cell, J. Power Sources 134 (1) (2004) 33–40.
[6] A. Hakenjos, H. Muenter, U. Wittstadt, C. Hebling, A PEM fuel cell for combined measurement of current and temperature, and flow field flooding, J. Power Sources 131 (2004) 213–216.
[7] X.G. Yang, F.Y. Zhang, A.L. Lubaway, C.Y. Wang, Visualization of liquid water transport in a PEFC, Electrochem. Solid State Lett. 7 (2004) A408–A411.
[8] S. Tsushima, K. Teranishi, S. Hirai, Magnetic resonance imaging of the water distribution within a polymer electrolyte membrane in fuel cells, Electrochem. Solid State Lett. 7 (9) (2004) A269–A272.
[9] K.W. Feindel, L.P.-A. LaRocque, D. Starke, S.H. Bergens, R.E. Wasylishen, In situ observations of water production and distribution in an operating H_2/O_2 PEM fuel cell assembly using ^1H NMR microscopy, J. Am. Chem. Soc. 126 (37) (2004) 11436–11437.
[10] R. Satija, D.L. Jacobson, M. Arif, S.A. Werner, In situ neutron imaging technique for evaluation of water management systems in operating PEM fuel cells, J. Power Sources 129 (2) (2004) 238–245.
[11] D. Kramer, J. Zhang, R. Shimoi, E. Lehmann, A. Wokaun, K. Shinohara, G. Scherer, In situ diagnostic of two-phase flow phenomena in polymer electrolyte fuel cells by neutron imaging. Part a. Experimental, data treatment, and quantification. Electrochim. Acta 50 (13) (2005) 2603–2614.
[12] N. Pekula, K. Heller, P.A. Chuang, A. Turhan, M.M. Mench, J.S. Brenizer, K. Ünlü, Study of water distribution and transport in a polymer electrolyte fuel cell using neutron imaging, Nucl. Instrum. Methods Phys. Res. Sect. A 542 (1–3) (2005) 134–141.
[13] Z.H. Wang, C.-Y. Wang, K.S. Chen, Two-phase flow and transport in the air cathode of proton exchange membrane fuel cells, J. Power Sources 94 (2001) 40–50.
[14] L. You, H. Liu, A two-phase and transport model for the cathode of PEM fuel cells, Int. J. Heat Mass Transf. 45 (2002) 2277–2287.
[15] T. Berning, N. Djilali, A 3D, multiphase, multicomponent model of the cathode and anode of a PEM fuel cell, J. Electrochem. Soc. 150 (12) (2003) A1589–A1598.

[16] G. Lin, W. He, T.V. Nguyen, Modeling liquid water effects in the gas diffusion and catalyst layers of the cathode of a PEM fuel cell, J. Electrochem. Soc. 151 (12) (2004) A1999–A2006.
[17] K.S. Udell, Heat transfer in porous media considering phase change and capillarity-the heat pipe effect, Int. J. Heat Mass Transf. 28 (2) (1985) 485–495.
[18] S. Litster, N. Djilali, Two-phase transport in porous gas diffusion electrodes, in: M. Faghri, B. Sunden (Eds.), Transport Phenomena in Fuel Cells, Developments in Heat Transfer, vol. 17, WIT Press, Southhampton, UK, 2005.
[19] S. Litster, G. McLean, PEM fuel cell electrodes, J. Power Sources 130 (2004) 61–76.
[20] M. Mathias, J. Roth, J. Fleming, W. Lehnert, Diffusion media materials and characterization. Handbook of Fuel Cells, John Wiley & Sons, Ltd., New York, 2003.
[21] J. Ihonen, M. Mikkola, G. Lindbergh, Flooding of gas diffusion backings in pefcs, J. Electrochem. Soc. 151 (8) (2004) A1152–A1161.
[22] D. Sinton, Microscale flow visualization, Microfluid. Nanofluid. 1 (2004) 2–21.
[23] S.-J. Lee, G.-B. Kim, X-ray particle image velocimetry for measuring quantitative flow information inside opaque objects, J. Appl. Phys. 94 (5) (2003) 3620–3623.
[24] M.H. Oddy, J.G. Santiago, J.C. Mikkelsen, Electrokinetic instability micromixing, Anal. Chem. 73 (2001) 5822–5832.